# CHAPTER 2

## Design of multi-layer models of SPR sensor

Contents

## Chapter 2: Design of multi-layer models of SPR sensor

### 2.1 Introduction

This chapter provides a brief review of promising materials like Two- Dimensional (2D) nanomaterials such as graphene, Blue Phosphorus (BlueP), Black Phosphorous (BP), Transition Metal Dichalcogenides (TMDCs), metal oxides etc. in the design of multi-layer mathematical models of SPR sensors. Thereafter the chapter presents the design of SPR sensors based on the multi-layer mathematical models exploring an optimal combination of novel materials with appropriate design parameters such as Refractive Index (RI), layer thickness etc. for plasmonic performance enhancement. The performance parameters of the SPR sensors viz, Sensitivity, Full Width at Half Maximum (FWHM) and Quality Factor (QF) are evaluated at an operating wavelength of 633 nm for RI range of 1.33-1.335 RIU of the sensing medium. The effect of the design parameters on the performance parameters of the SPR sensors is studied in detail. A comparative study of the performances of the various SPR designs is presented elaborately.

The design of a conventional Kretschmann configured SPR sensor is based on a three-layer mathematical model consisting of a prism, a metal layer such as gold (Au), silver (Ag) etc. and a dielectric medium. However, over the years, a lot of research has been directed towards designing of SPR sensors based on multi-layer (more than three) mathematical models using novel materials for further enhancement of SPR sensing performance. The use of the right combination of promising materials is expected to facilitate stronger plasmonic coupling due to better optical absorption capacity, adhesive property, molecular adsorption capacity etc. In the last two decades, 2D nanomaterials such as graphene, BlueP, TMDCs like Molybdenum Disulfide ($MoS_2$), Molybdenum Diselenide ($MoSe_2$), Tungsten Disulfide ($WS_2$) etc. have gained a lot of attention due to their excellent optical and electrical properties [1-4]. 2D nanomaterials are a family of very thin layered materials with high planar and anisotropic architecture. The planar topography of 2D nanomaterials imparts desirable characteristics such as a very high surface-to-volume ratio, superior functionalization capabilities, good mechanical properties etc. suited for various applications. 2D nanomaterials have the highest specific surface area, compared to other nanomaterials, such as 1D or 3D nanomaterials, resulting in a high number of surface atoms compared to volume atoms. The presence of large number of surface atoms provides high surface energy and a high number of surface anchoring sites resulting in enhanced interactions of 2D nanomaterials with biomolecules, particularly suited for biosensing applications. In recent years, heterostructures of 2D nanomaterials have been reported for sensitivity improvement of SPR biosensors [5-7]. 2D nanomaterials such as TMDCs and their heterostructures can absorb higher light energy due to their large real part of the dielectric constant than the metal layer, thus facilitating stronger excitation of Surface Plasmons (SPs) compared to conventional SPR sensors. In addition to that, they also induce a strong coupling at

the metal/TMDCs interface enhancing the electric field. The enhanced electric field is extremely sensitive to the refractive index changes of the analyte resulting in improved sensitivity of the sensor [8, 9]. Specifically, BlueP/TMDC based heterostructures, viz, BlueP-$MoS_2$, BlueP-$MoSe_2$, BlueP-$WS_2$ and BlueP-$WSe_2$ are reported to have high energy bandgap, charge transfer, work function and optical absorption capacity. In addition, from an experimental synthesis point of view, BlueP/TMDC based heterostructures have low interlayer lattice mismatches of +3.18% (BlueP-$MoS_2$), −0.82% (BlueP-$MoSe_2$), +3.15% (BlueP-$WS_2$) and −0.82% (BlueP-$WSe_2$). Moreover, the negative formation energies of −165.6 meV/unit-cell (BlueP-$MoS_2$), −210.5 meV/unit-cell (BlueP-$MoSe_2$), −161.2 meV/unit-cell (BlueP-$WS_2$) and −209.7 meV/unit-cell (BlueP-$WSe_2$) indicate their thermodynamic stability. The binding energies between BlueP and TMDCs monolayer heterostructures are 16.11 meV/Å$^2$ (BlueP-$MoS_2$), 19.46 meV/Å$^2$ (BlueP-$MoSe_2$), 15.69 meV/Å$^2$ (BlueP-$WS_2$) and 19.38 meV/Å$^2$ meV/Å$^2$ (BlueP-$WSe_2$) which are compatible with the Density Functional Theory (DFT) estimated Van Der Waals (vdW) binding energy value of 20 meV/Å$^2$ [10].

Apart from 2D nanomaterials and their heterostructures, high RI metal oxides such as Titanium Dioxide ($TiO_2$), Indium Tin Oxide (ITO), Silicon Dioxide ($SiO_2$), Zinc Oxide (ZnO) etc. have received significant attention as adhesive layers for uplifting SPR performance [11, 12]. The transition metals such as Chromium (Cr) or Titanium (Ti), which are commonly used to improve the adhesion between plasmonic metal and glass substrate usually produce large FWHM, metal interdiffusion and have low light trapping capacity [13]. The high RI metal oxides in combination with plasmonic metals such as Au, Ag etc. support strong excitation of SPs at metal-glass interface boosting the performance of SPR sensors. Further, the RI of the glass prism also has a notable effect on the performance of the SPR sensors [14]. Therefore the right combination of 2D nanomaterials and their heterostructures, metal oxides, prisms etc. is critical for the suitable design of multi-layer mathematical models of SPR sensors for improved sensing performance.

## 2.2 Methodology

The multi-layer mathematical models of SPR sensors are developed based on the Transfer Matrix Method (TMM) and Fresnel Multilayer Reflection Theory [1]. The basic

structure of a conventional Kretschmann configured SPR sensor based on a three-layer mathematical model consists of a prism at the base followed by a metal layer and a dielectric. The prism is used to couple the incident p-polarized light to the SPs travelling along the metal-dielectric interface. For the design of SPR sensors based on multi-layer mathematical models, novel materials like 2D nanomaterials and their heterostructures are stacked layer wise over the metal film such as Au to facilitate stronger excitation of SPs. Further, the metal oxides are used as adhesive layers sandwiched between the prism and Au layer to help in the effective trapping of the incident light for improved SPR sensing. In this research, an optimal choice of materials with appropriate design parameters viz, RI, Layer thickness etc. are studied in detail to design SPR sensors based on multi-layer mathematical models with a superior plasmonic response. Three SPR sensors were designed based on the three-layer (Design I), four-layer (Design II) and five-layer (Design III) mathematical models, as illustrated in Figure 2.1, using a MATLAB simulation programme and analyzed using a graphical analysis approach. The performance parameters of the sensors viz, Sensitivity, FWHM and QF were evaluated at an operating wavelength of 633 nm for RI change in the range 1.33-1.335 RIU. The effect of the design parameters on the SPR performance parameters was analyzed. A comparative study of the three SPR sensors was also performed.

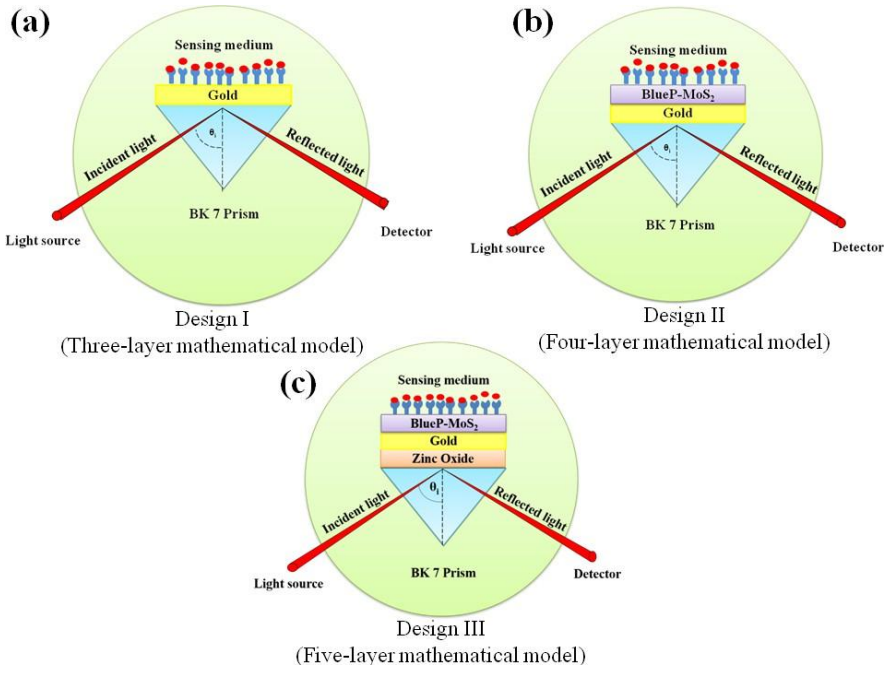


Figure 2.1: Schematic representation of SPR sensors a) Design I b) Design II c) Design III based on three-layer, four-layer and five-layer mathematical models respectively

### 2.2.1 Mathematical modelling of SPR sensor

The propagation constant ($K_{SP}$) of the Surface Plasmon Wave (SPW), which is the electron density wave propagating along the interface of metal and dielectric, is given as [15]:

$$K_{SP} = \frac{\omega}{c}\left[\sqrt{\frac{\epsilon_M \epsilon_s}{\epsilon_M + \epsilon_s}}\right] \quad (2.1)$$

where ω is the frequency of the incident light, $c$ is the velocity of light, $\epsilon_M$ and $\epsilon_S$ represent the dielectric constants of the metal layer and dielectric medium, respectively.

The p-polarized light incident on the prism-metal layer interface through the prism at an angle equal to or greater than the angle required for Attenuated Total Reflection (ATR), generates an evanescent wave, whose propagation constant ($K_{ev}$) is given as:

$$K_{ev} = \frac{\omega}{c} n_p sin\theta \ (2.2)$$

where $\theta$, $\omega$, $c$ and $n_p$ are the angle of incidence of light, frequency of light, speed of light and the RI of the glass prism respectively.

For the excitation of SPs, the propagation constant of the SPW ($K_{SP}$) should match with that of the evanescent wave ($K_{ev}$), the corresponding resonance condition of which is given by:

$$\frac{\omega}{c} n_p sin\theta_{SPR} = \frac{\omega}{c}\left[\sqrt{\frac{\epsilon_M \epsilon_s}{\epsilon_M + \epsilon_s}}\right] \quad (2.3)$$

where $\Theta_{SPR}$ is the resonance angle.

The dielectric constant of the metal (Au) layer is determined using the Drude-Lorentz model which establishes a relationship between the metal's dielectric constant ($\epsilon_M$) at wavelength ($\lambda$), given as [16]:

$$\epsilon_m\ (\lambda) = 1 - \left[\frac{\lambda^2 \lambda_C}{(\lambda_C + i\lambda)\lambda_p^2}\right] \quad (2.4)$$

where, $\lambda_p$ ($1.68 \times 10^{-7}$ m) and $\lambda_c$ ($8.93 \times 10^{-6}$ m) are the plasma wavelength and the collision wavelength of gold respectively.

The tangential components of electromagnetic field boundary are given as [17]:

$$\begin{pmatrix} P_1 \\ Q_1 \end{pmatrix} = X_1 X_2 X_3 X_4 X_5 \ldots\ldots\ldots\ldots\ldots\ldots X_{N-1} \begin{pmatrix} P_{N-1} \\ Q_{N-1} \end{pmatrix} = X \begin{pmatrix} P_{N-1} \\ Q_{N-1} \end{pmatrix} \quad (2.5)$$

Here, $P_1$, $Q_1$ and $P_{N-1}$, $Q_{N-1}$ are tangential components of electric field and magnetic field respectively at first and final layer interface. $X$, is the characteristic matrix with elements $Xij$, defined as:

$$X = \begin{bmatrix} x_{11} & x_{12} \\ x_{21} & x_{22} \end{bmatrix} = \prod_{k=2}^{N-1} X_k \quad (2.6)$$

$$\text{with } X_k = \begin{bmatrix} \cos\beta_k & -i\sin\beta_k/q_k \\ -iq_k\sin\beta_k & \cos\beta_k \end{bmatrix} \quad (2.7)$$

where, $k$ represents an arbitrary number, while $\beta_k$ and $q_k$ represent the phase thickness and refractive indices of the corresponding layers, and $x_{11}$, $x_{12}$, $x_{21}$ and $x_{22}$ represent the transfer matrix elements, respectively. $q_k$ and $\beta_k$ are defined as:

$$q_k = \left[\frac{(\in_k - n_p^2\sin^2\theta)^{\frac{1}{2}}}{\in_k}\right], \beta_k = \frac{2\pi d_k}{\lambda}\left[(\in_k - n_p^2\sin^2\theta)^{\frac{1}{2}}\right] \quad (2.8)$$

where $\in_k$ and $d_k$ represent the permittivity and thickness of the k$^{th}$ layer respectively.

Based on the above measures, the amplitude of the reflection coefficient ($r$) and reflectivity ($R_P$) for incident p-polarized light can be calculated as follows:

$$R_p = |r|^2 = \left[\frac{(x_{11}+x_{12}q_N)q_1 - (x_{21}+x_{22}q_N)}{(x_{11}+x_{12}q_N)q_1 + (x_{21}+x_{22}q_N)}\right] \quad (2.9)$$

### 2.2.2 Performance parameters of SPR sensor

The performance of a Kretschmann angular configured SPR sensor is evaluated using three key performance parameters viz, Sensitivity, FWHM and QF as listed below.

The sensitivity (S) of an SPR sensor in the Kretschmann angular interrogation configuration is defined as the ratio of the shift in the resonance angle ($\Delta\Theta_{res}$) to the change in RI ($\Delta n$) of the sensing medium and represented as follows [18]:

$$S = \frac{\Delta\Theta}{\Delta n} \quad (2.10)$$

It is expressed in ˚/RIU. The sensitivity of the SPR sensor is calculated for $\Delta n$=0.005 RIU using equation 2.10.

The FWHM of an SPR sensor is the spectral width of the SPR curve at half value of the maximum reflectance. The FWHM of an SPR curve is evaluated by calculating the width of the SPR curve correspondingly at half the value of the maximum reflectance [19]. It is expressed in degree (˚). A narrow SPR reflectance curve has low FWHM which indicates good detection accuracy of the sensor.

The QF of an SPR sensor is expressed as the ratio of the sensitivity to the FWHM and is represented as [20]:

$$\mathrm{QF} = \frac{\mathrm{S}}{\mathrm{FWHM}} \tag{2.11}$$

It is expressed in $\mathrm{RIU}^{-1}$. The QF of the SPR sensor is calculated using equation 2.11.

### 2.2.3 Design parameters

The parameters for the design of multi-layer mathematical models of SPR sensors are viz; RI, excitation wavelength and thickness.

#### 2.2.3.1 RI

**a) Glass prism**

BK7 glass with a RI of 1.515 (at 633 nm wavelength) is used as the choice of glass for the prism to match the momentum of the incident light to that of the SPs. The BK7 prism is preferred because of its higher sensitivity over high RI prisms like SF10 and SF11 and better measurement precision over low RI prisms like $CaF_2$, FK51A etc. [14].

**b) Metal**

Au with a RI of 0.16172+3.21182i (at 633 nm wavelength) is preferred as the metal layer as it demonstrates a higher shift in the resonance angle due to the change in RI of the sensing layer in comparison to Ag, Copper (Cu), etc. Although Ag and Au exhibit sharper resonance signals resulting in greater measurement accuracy and are also cost-effective, they are prone to oxidation. Au, on the other hand, is chemically stable thereby enhancing the performance and longevity of the SPR sensor [21].

**c) 2D nanomaterials**

The RI of different 2D nanomaterials and their heterostructures considered in the modelling are enlisted in Table 2.1 [22-23].

Table 2.1: RI of different 2D nanomaterials at 633 nm

| 2D nanomaterials | RI (at 633 nm) |
|---|---|
| Graphene | 3.0 + 1.1487i |
| $MoS_2$ | 5.0805 +1.1724i |
| $WS_2$ | 4.8937 +0.3123i |
| $MoSe_2$ | 4.6226 +1.0062i |
| $WSe_2$ | 4.5501 +0.4332i |
| Mxene | 2.38 + 1.33*i* |
| BlueP-$MoS_2$ | 2.810 + 0.320i |
| BlueP-$WS_2$ | 2.480 + 0.170i |
| BlueP-$MoSe_2$ | 2.770 + 0.350i |
| BlueP-$WSe_2$ | 2.680 + 0.220i |

**d) Metal oxide**

ZnO with a RI of 1.952 + 0.02i (at 633 nm wavelength) is used as an adhesion layer between the BK7 prism and Au [24]. The BK7 and Au surface show weak adhesion, leaving the scope of sensitivity degradation. The ZnO layer on the top of the BK7 prism is used to improve the adhesion between the layers. The high optical transparency and high luminescence of ZnO over conventional adhesive materials such as Cr or Ti [25-27], help in the trapping of incident light to promote the generation of more SPs, thereby increasing the plasmonic effect [28].

**e) Sensing medium**

The sensing medium chosen is an aqueous solution having RI in the range 1.330-1.335. The adsorption of biomolecules on the sensing surface changes the carrier concentration of the aqueous solution thereby resulting in modification of the RI of the sensing medium.

### 2.2.3.2 Excitation wavelength

Monochromatic light of wavelength 633 nm is used as the incident light for the excitation of SPs for all the multi-layer mathematical models. This is because optical

nonlinearity increases at high frequencies and the overall sensitivity of the sensor is enhanced with minimum Kerr effect [16].

#### 2.2.3.3 Layer thickness

The thicknesses of the Au, 2D nanomaterials and their heterostructures and metal oxide layers are considered for the design of different multi-layer mathematical models of SPR sensors.

## 2.3 Results and Discussion

### 2.3.1 Effect of different materials and their thicknesses on the SPR performance parameters

#### 2.3.1.1 Design I

The Design I of SPR sensor is based on a three-layer mathematical model consisting of BK7 prism, Au and sensing medium. The SPR performance parameters of Design I are evaluated from the SPR reflectance curves plotted for different thicknesses of the Au layer. Figure 2.2 illustrates some of the SPR reflectance curves plotted for gold thickness varying from 35 nm to 55 nm. The effect of the variation of thickness of the Au layer on the SPR performance parameters of Design I is presented in Figure 2.3. As seen from the figure, the sensitivity of the SPR sensor increases significantly from 136˚/RIU to 172˚/RIU with an increase in Au thickness from 35 nm to 55 nm. It is also observed from the figure that the FWHM of the SPR sensor decreases appreciably from 7.67656˚ to 4.26311˚ with an increase in Au thickness from 35 nm to 55 nm, thus leading to improvement in the detection accuracy of the SPR sensor. Further, it is also noted from the figure that the QF of the SPR sensor also improves largely from 17.72 $RIU^{-1}$ to 40.35 $RIU^{-1}$ with an increase in the thickness of Au. Thus, 55 nm is the optimum thickness of Au for Design I producing sensitivity, FWHM and QF of 172˚/RIU, 4.26311˚ and 40.35 $RIU^{-1}$ respectively. For further designs, the thicknesses of the individual layers are so chosen that the effective thickness of the stacked layers in the SPR sensor is ~55 nm.

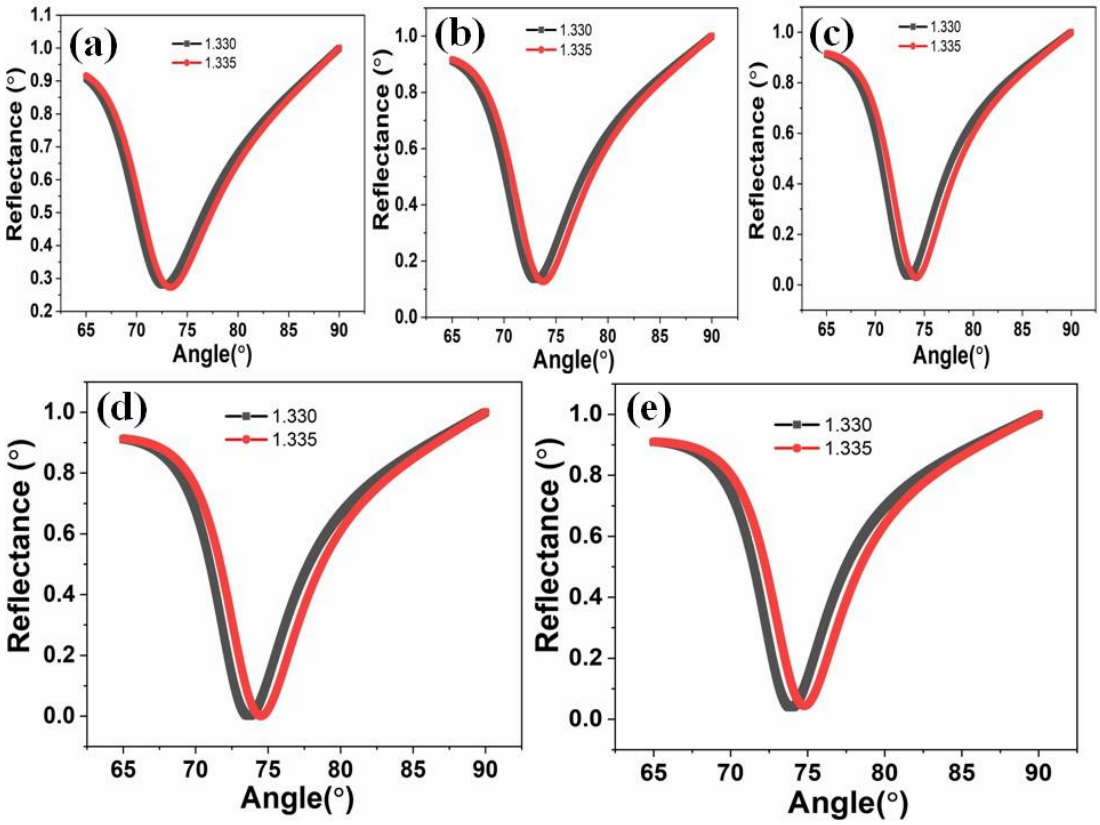


Figure 2.2: SPR reflectance curves of Design I for different thicknesses of Au layer (a) 35 nm (b) 40 nm (c) 45 nm (d) 50 nm (e) 55 nm

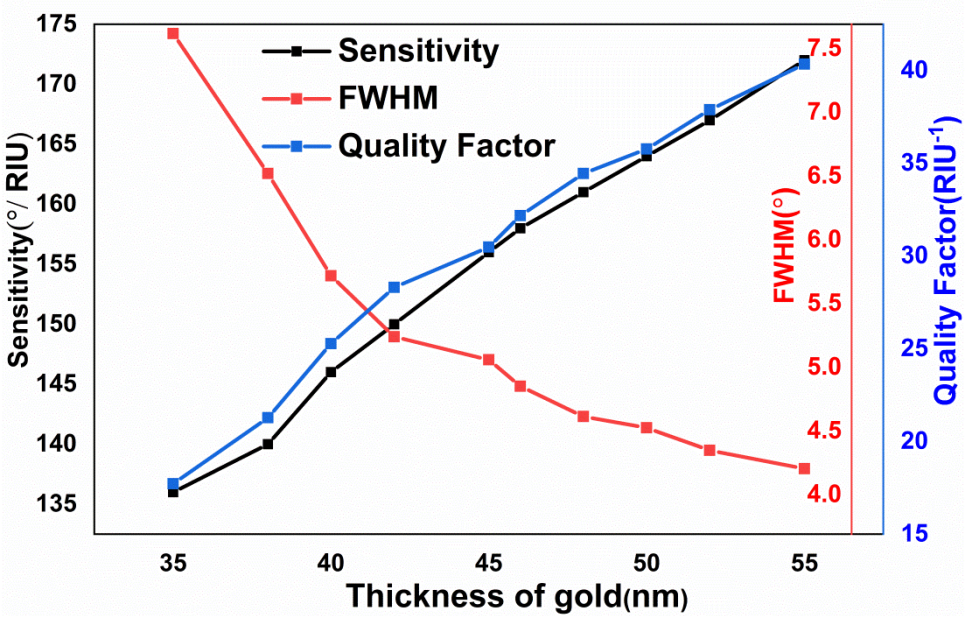


Figure 2.3: Variation of SPR performance parameters for Design I with different thicknesses of Au

### 2.3.1.2 Design II

Design II of the SPR sensor is based on a four-layer mathematical model considering different 2D nanomaterials above the Au layer. Table 2.2 enlists the monolayer thickness of different 2D nanomaterials considered in the Design II of the SPR sensor [22, 23]. Table 2.3 enlists the performance parameters of the SPR sensor for Design II considering different 2D nanomaterials. The thickness of the Au film is fixed at 54 nm for this study.

Table 2.2: Monolayer thickness of different 2D nanomaterials at 633 nm

| 2D nanomaterials | Monolayer thickness (nm) |
|---|---|
| Graphene | 0.34 |
| $MoS_2$ | 0.65 |
| $WS_2$ | 0.80 |
| $MoSe_2$ | 0.70 |
| $WSe_2$ | 0.70 |
| MXene | 0.993 |
| BlueP-$MoS_2$ | 0.75 |
| BlueP-$WS_2$ | 0.75 |
| BlueP-$MoSe_2$ | 0.78 |
| BlueP-$WSe_2$ | 0.78 |

The SPR resonance shift is associated with the real part of the dielectric constant of a material and hence the real part of the RI. It is high for a material with a larger real part of the dielectric constant inevitably resulting in higher sensitivity [21]. It is observed from Table 2.3 that the sensitivity increases with an increase in the number of layers of the 2D nanomaterials due to the effective increase of the real part of the RI and hence the real part of the dielectric constant. A monolayer of graphene has a relatively small value of the real part of the RI and produces a low sensitivity of 182˚/RIU in comparison to the TMDC nanomaterials, viz; $MoS_2$ (216˚/RIU), $WS_2$ (230˚/RIU), $MoSe_2$ (212˚/RIU) and $WSe_2$ (212˚/RIU). The monolayers of the TMDC nanomaterials also show higher sensitivities than the monolayer of MXene (194˚/RIU) and monolayers of heterostructures viz, BlueP-$MoS_2$ (192˚/RIU), BlueP-$WS_2$ (188˚/RIU), BlueP-$MoSe_2$ (192˚/RIU) and BlueP-$WSe_2$ (192˚/RIU) due to their relatively larger values of the real part of the RI. However, for a few layered TMDCs, the sensitivity calculation was not possible due to the broadening of the SPR curve resulting from the high damping of SPs [29]. A five-layer graphene produces a maximum sensitivity of 228˚/RIU. Trilayers of Mxene, in spite of a small real part of the RI of 2.38, produce a significantly high sensitivity of 248˚/RIU due to its high monolayer thickness. Multi-layers of Blue P and

Table 2.3: Performance parameters of SPR sensor for Design II considering different 2D nanomaterials

| **Performance Parameters** | **Thickness of Au (nm)** | **No. of layers of 2D nano-materials** | **Graphene** | **$MoS_2$** | **$WS_2$** | **$MoSe_2$** | **$WSe_2$** | **MXene** | **BlueP-$MoS_2$** | **BlueP-$WS_2$** | **BlueP-$MoSe_2$** | **BlueP-$WSe_2$** |
|---|---|---|---|---|---|---|---|---|---|---|---|---|
| **Sensitivity (°/RIU)** | 54 | 1 | 182 | 216 | 227 | 212 | 212 | 194 | 192 | 188 | 192 | 192 |
| | | 2 | 192 | --- | --- | --- | --- | 220 | 216 | 206 | 216 | 212 |
| | | 3 | 202 | --- | --- | --- | --- | 248 | 250 | 230 | 248 | 246 |
| | | 5 | 228 | --- | --- | --- | --- | --- | --- | --- | --- | --- |
| | | 7 | --- | --- | --- | --- | --- | --- | --- | --- | --- | --- |
| **FWHM(°)** | 54 | 1 | 4.0331 | 5.5002 | 4.7634 | 5.2812 | 4.9458 | 5.0573 | 4.0664 | 3.8592 | 4.1185 | 3.9681 |
| | | 2 | 4.6460 | --- | --- | --- | --- | 6.3314 | 4.7560 | 4.3443 | 4.9001 | 4.5758 |
| | | 3 | 5.2238 | --- | --- | --- | --- | 6.7999 | 5.3985 | 4.8633 | 5.4874 | 5.1619 |
| | | 5 | 6.1786 | --- | --- | --- | --- | --- | --- | --- | --- | --- |
| | | 7 | --- | --- | --- | --- | --- | --- | --- | --- | --- | ---- |
| **QF ($RIU^{-1}$)** | 54 | 1 | 45.12 | 39.27 | 47.65 | 40.14 | 42.86 | 38.36 | 47.21 | 48.71 | 46.61 | 48.38 |
| | | 2 | 41.32 | --- | --- | --- | --- | 34.75 | 45.42 | 47.41 | 44.08 | 46.33 |
| | | 3 | 38.67 | --- | --- | --- | --- | 36.47 | 46.30 | 47.29 | 45.19 | 47.65 |
| | | 5 | 36.90 | --- | --- | --- | --- | --- | --- | --- | --- | --- |
| | | 7 | --- | --- | --- | --- | --- | --- | --- | --- | --- | --- |

TMDC combinations show better sensitivities than graphene and TMDCs due to the effective increase in real part of the RI at trilayer thickness. BlueP-$MoS_2$ heterostructure with a real part of the RI of 2.810 exhibits the highest sensitivity of 250˚/RIU over other BlueP/TMDC combinations at trilayer. The trilayers of other combinations; BlueP-$WS_2$, BlueP-$WSe_2$ and BlueP-$MoSe_2$, with the real part of the RI of 2.480, 2.680 and 2.770 respectively exhibit sensitivities of 230˚/RIU, 246˚/RIU and 248˚/RIU respectively. However, for multi-layered graphene (beyond five-layer), Mxene (beyond trilayer) and BlueP/TMDC based heterostructures (beyond trilayer), the sensitivities could not be calculated due to the broadening of the SPR curves resulting from the high damping of SPs.

The FWHM of the SPR curve, which determines the detection accuracy of the SPR sensor is associated with the imaginary part of the dielectric constant and hence the extinction coefficient of the material [21]. The FWHM of an SPR sensor is low for a material with a smaller imaginary part of the dielectric constant. It is observed from Table 2.3 that with an increase in the number of layers of the 2D nanomaterials, the FWHM increases. This is due to the effective increase in the extinction coefficient and hence the imaginary part of the dielectric constant as a result of which the plasmonic damping is amplified leading to the broadening of the SPR curves [29]. Five-layer graphene, with a large extinction coefficient of 1.1487, produces a high FWHM of 6.17861˚ beyond which the FWHM could not be calculated due to increased damping of SPs. Monolayer of $WS_2$ with an extinction coefficient of 0.3123 produces the least FWHM of 4.763415˚ over other TMDC nanomaterials. Monolayers of other TMDCs; $WSe_2$, $MoSe_2$ and $MoS_2$ with extinction coefficients of 0.4332, 1.0062 and 1.1724 respectively produce FWHM of 4.945895˚, 5.28127˚ and 5.50026˚ respectively. MXene has the largest value of extinction coefficient among the 2D nanomaterials and the trilayer of MXene produces the highest FWHM of 6.79993˚ compared to other 2D nanomaterials. BlueP-$WS_2$ heterostructure with an extinction coefficient of 0.17 exhibits the least FWHM of 4.86336˚ over other BlueP/TMDC combinations at trilayer. The trilayers of other combinations; BlueP-$WSe_2$, BlueP-$MoS_2$ and BlueP-$MoSe_2$, with extinction coefficients of 0.22, 0.32 and 0.35 respectively exhibit FWHM of 5.16191˚, 5.39856˚ and 5.48745˚ respectively. However, beyond trilayer, the FWHM for TMDCs, Mxene and BlueP/TMDC based heterostructures, could not be calculated due to the

effective increase in the extinction coefficient resulting in the broadening of the SPR curves due to increased damping of SPs.

Table 2.3 illustrates that monolayer graphene exhibits a decent QF of 45.12 $RIU^{-1}$ which deteriorates to 36.90 $RIU^{-1}$ for five layers due to the increase in FWHM from 4.0331˚(monolayer) to 6.17861˚(five-layer). Monolayers of TMDC nanomaterials; $MoS_2$, $WS_2$, $MoSe_2$ and $WSe_2$ produce QF of 39.27 $RIU^{-1}$, 47.2 $RIU^{-1}$, 40.14 $RIU^{-1}$ and 45.14 $RIU^{-1}$ respectively. The trilayer of Mxene exhibits a poor QF of 36.47 $RIU^{-1}$ due to its large FWHM. Comparatively, trilayers of BlueP-$MoS_2$, BlueP-$WS_2$, BlueP-$MoSe_2$ and BlueP-$WSe_2$ exhibit relatively high QF of 46.30 $RIU^{-1}$, 47.29 $RIU^{-1}$, 45.19 $RIU^{-1}$ and 47.65 $RIU^{-1}$ respectively.

From the above discussion, it may be concluded that BlueP-$MoS_2$ produces the highest sensitivity among all the 2D nanomaterials and also exhibits a relatively high QF and low FWHM. The low interlayer lattice mismatches of 3.168% of BlueP-$MoS_2$ and the hexagonal lattice structures of monolayers of both BlueP and $MoS_2$ support the experimental synthesis of the heterostructure [10, 30]. Furthermore, the strong biomolecular adsorption capacity of BlueP-$MoS_2$ helps build a strong electromagnetic field at the metal-dielectric interface, beneficial for improving the sensitivity of the SPR sensor [31]. Thus the favourable material property of the two individual components (BlueP and $MoS_2$) strongly supports their candidature for the formation of a promising heterostructure material for plasmonic enhancement. Therefore, BlueP-$MoS_2$ heterostructure is considered as the choice of the 2D nanomaterial layer for Design II of the SPR sensor and further considerations.

Similar to Figure 2.2, the SPR performance parameters of Design II are evaluated from the SPR reflectance curves, plotted for different thicknesses of BlueP-$MoS_2$ heterostructure layer from monolayer (0.75 nm) to trilayer (3 x 0.75 nm). The variation of the SPR performance parameters of Design II with the number of layers of BlueP-$MoS_2$ is illustrated in Figure 2.4. As evident from the figure, the sensitivity of the SPR sensor increases from 192˚/RIU to 250˚/RIU with an increase in the number of layers of BlueP-$MoS_2$ from monolayer to trilayer. It is also observed from the figure that the QF incurs a very minimal decrement from 47.21 $RIU^{-1}$ to 46.30 $RIU^{-1}$ with an increase in the number of layers of BlueP-$MoS_2$ from monolayer to trilayer despite an increment of

the FWHM from 4.0664˚ to 5.398560˚. Thus, the trilayer (3 x 0.75 nm) of BlueP-$MoS_2$ is the optimum thickness for Design II producing sensitivity, FWHM and QF of 250˚/RIU, 5.398560˚ and 46.30 $RIU^{-1}$ respectively.

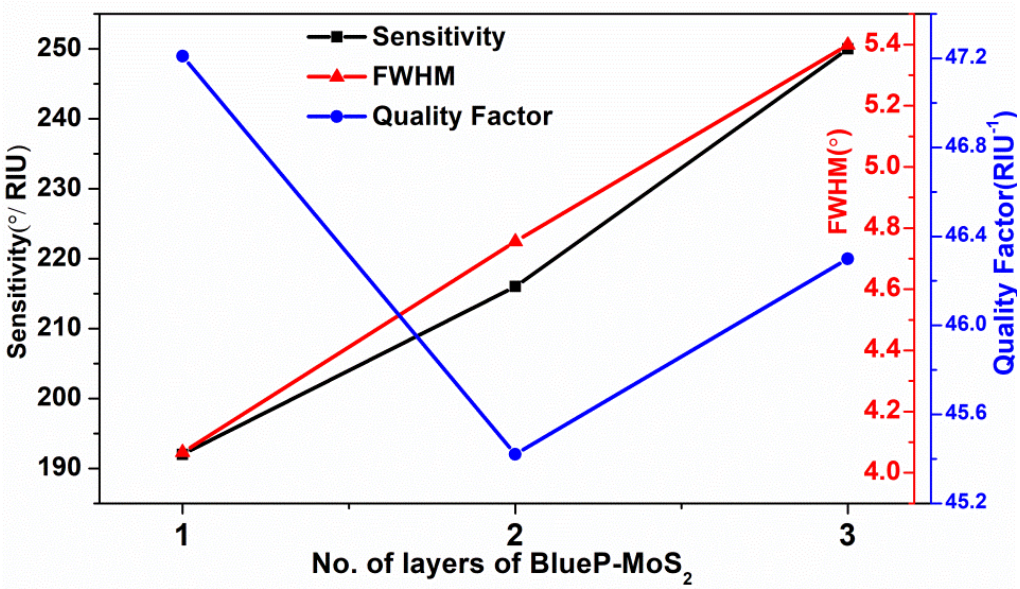


Figure 2.4: Variation of SPR performance parameters for Design II with the number of layers of BlueP-$MoS_2$

### 2.3.1.3 Design III

The Design III of the SPR sensor is based on a five-layer mathematical model considering an adhesive layer of ZnO between the BK7 prism and Au. Table 2.4 enlists the performance parameters of the SPR sensor for Design III considering different thicknesses of ZnO (3 nm to 9 nm) with three thicknesses of Au (45 nm, 48 nm and 50 nm) and BlueP-$MoS_2$ heterostructure (from monolayer to five layers).

It is observed in general from Table 2.4 that for monolayer and bilayer BlueP-$MoS_2$, SPR sensitivity increases up to a critical ZnO thickness beyond which the sensitivity starts decreasing. Design III produces the highest sensitivity of 260˚/RIU with 48 nm Au, 6 nm thickness of ZnO and monolayer of BlueP-$MoS_2$ which is superior to Design I and II. The ZnO with a high real part of the RI results in an effective increase in the real part of the dielectric constant at an optimal ZnO thickness of 6 nm with 48 nm Au and monolayer BlueP-$MoS_2$ which is attributed to improved sensitivity. Beyond bilayer BlueP-$MoS_2$, SPR sensitivity does not show any improvement with an increase in

Table 2.4: Performance parameters of SPR sensor for Design III considering different thicknesses of ZnO

| Performance Parameters | Thickness of ZnO (nm) | 45nm Au | | | | 48nm Au | | | | 50nm Au | | | |
|---|---|---|---|---|---|---|---|---|---|---|---|---|---|
| | | BlueP-$MoS_2$ | | | | BlueP-$MoS_2$ | | | | BlueP-$MoS_2$ | | | |
| | | Mono layer | Bilayer | Tri layer | Five layer | Mono layer | Bilayer | Tri layer | Five layer | Monolayer | Bilayer | Tri layer | Five layer |
| **Sensitivity (°/RIU)** | 3 | 200 | 220 | 220 | 140 | 220 | 220 | 220 | 80 | 220 | 240 | 240 | 60 |
| | 4 | 220 | 240 | 220 | 30 | 240 | 240 | 220 | 20 | 220 | 240 | 180 | 0 |
| | 5 | 220 | 240 | 200 | 0 | 240 | 220 | 140 | -20 | 246 | 220 | 120 | -40 |
| | 6 | 240 | 220 | 120 | -20 | 260 | 180 | 80 | -60 | 240 | 160 | 40 | -60 |
| | 7 | 250 | 180 | 40 | -60 | 240 | 100 | 0 | -- | 200 | 80 | -20 | -- |
| | 8 | 220 | 60 | -20 | -60 | 140 | 20 | -60 | -- | 100 | -20 | -40 | -- |
| | 9 | 100 | 0 | -40 | -60 | 40 | -40 | -60 | -- | 0 | -60 | -80 | -- |
| **FWHM (°)** | 3 | 5.0356 | 6.1058 | 7.7379 | 9.8236 | 4.4832 | 6.7486 | 8.1965 | 9.9744 | 5.5883 | 7.0035 | 8.3833 | 9.9196 |
| | 4 | 5.6826 | 7.0401 | 8.4112 | 10.2651 | 4.8962 | 7.4804 | 8.7191 | 10.2268 | 6.5009 | 7.7120 | 8.8412 | 10.1187 |
| | 5 | 6.4187 | 7.7086 | 8.9150 | 10.5921 | 4.9523 | 8.1480 | 9.1122 | 10.4256 | 7.4429 | 8.2609 | 9.1882 | 10.2235 |
| | 6 | 7.1017 | 8.3878 | 9.3616 | 10.8509 | 5.4012 | 8.6036 | 9.4608 | 10.4852 | 7.6985 | 8.6940 | 9.4668 | 10.2207 |
| | 7 | 7.6700 | 8.7713 | 9.7137 | 11.0662 | 6.0013 | 9.0110 | 9.6630 | -- | 8.2070 | 8.9441 | 9.6230 | -- |
| | 8 | 8.2919 | 9.3437 | 10.0920 | 10.7629 | 7.5389 | 9.2992 | 9.9158 | -- | 8.5699 | 9.2596 | 9.7155 | -- |
| | 9 | 8.8065 | 9.6378 | 10.3150 | 10.9339 | 7.9166 | 9.5325 | 9.9731 | -- | 8.9026 | 9.6796 | 9.8143 | -- |
| **QF ($RIU^{-1}$)** | 3 | 39.72 | 36.03 | 28.43 | 14.25 | 49.07 | 32.59 | 26.84 | 8.020 | 39.36 | 34.26 | 28.63 | 6.04 |
| | 4 | 38.71 | 34.09 | 26.15 | 2.92 | 49.01 | 32.08 | 25.23 | 1.96 | 33.84 | 31.12 | 20.36 | 0 |
| | 5 | 34.27 | 31.13 | 22.43 | 0 | 48.46 | 27.00 | 15.36 | --- | 33.05 | 26.63 | 13.06 | -- |
| | 6 | 33.79 | 26.22 | 12.81 | --- | 48.14 | 20.92 | 8.46 | --- | 31.17 | 18.40 | 4.23 | -- |
| | 7 | 32.59 | 20.52 | 4.12 | --- | 40 | 11.09 | 0 | --- | 24.36 | 8.94 | --- | -- |
| | 8 | 26.53 | 6.42 | -- | --- | 18.57 | 2.150 | --- | --- | 11.66 | --- | --- | -- |
| | 9 | 11.35 | 0 | -- | --- | 5.06 | -- | --- | --- | 0 | --- | --- | -- |

ZnO thickness. It is also observed from Table 2.4 that the FWHM increases with an increase in ZnO thickness for all layers of BlueP-$MoS_2$ (from monolayer to five-layer) and thicknesses of Au (45 nm, 48 nm and 50 nm). This is due to the effective increase in the extinction coefficient with an increase in ZnO thickness causing the high damping of SPs resulting in broadening of the SPR curves. Monolayer BlueP-$MoS_2$ with 48 nm Au exhibits the least FWHM of 4.48321˚ for 3 nm thickness of ZnO which rises to 7.916675˚ for 9 nm ZnO thickness. Table 2.4 also illustrates that the QF decreases with an increase in ZnO thickness for all layers of BlueP-$MoS_2$ (from monolayer to five-layer) and thicknesses of Au (45 nm, 48 nm and 50 nm) due to corresponding increase of the FWHM. Monolayer BlueP-$MoS_2$ with 48 nm Au exhibits the highest QF of 49.07 $RIU^{-1}$ for 3 nm thickness of ZnO which decreases marginally to 48.14 $RIU^{-1}$ for 6 nm ZnO thickness and drops to 5.06 $RIU^{-1}$ for 9 nm ZnO thickness.

The use of ZnO as an adhesive layer between the BK7 prism and Au surface thus produces a high resonance angle shift and smaller FWHM in the SPR curve leading to enhanced sensitivity, detection accuracy and improvement in the performance parameters of the sensor. Similar to Figure 2.2, the SPR performance parameters of Design III are evaluated from the SPR reflectance curves, plotted for different thicknesses of the ZnO layer from 3 nm to 9 nm, for monolayer BlueP-$MoS_2$ and 48 nm Au. The effect of the thickness of ZnO on the SPR performance parameters of Design III is illustrated in Figure 2.5. As seen from the figure, the sensitivity rises with an increase in ZnO thickness reaching a maximum value of 260˚/RIU for 6 nm ZnO beyond which the sensitivity decreases to 40˚/RIU for 9 nm ZnO. The FWHM rises steadily from 4.48321˚ to 5.40121˚ with an increase in ZnO thickness from 3 nm to 6 nm followed by a rapid increment reaching 7.916675˚ at 9 nm ZnO thickness. The QF of the SPR sensor, on the other hand, decreases very marginally from 49.07 $RIU^{-1}$ to 48.14 $RIU^{-1}$ with an increase in ZnO thickness from 3 nm to 6 nm beyond which it decreases rapidly falling to 5.06 $RIU^{-1}$ for 9 nm ZnO. Thus, 6 nm is the optimum ZnO thickness for Design III producing sensitivity, FWHM and QF of 260˚/RIU, 5.40121˚and 48.14 $RIU^{-1}$ respectively.

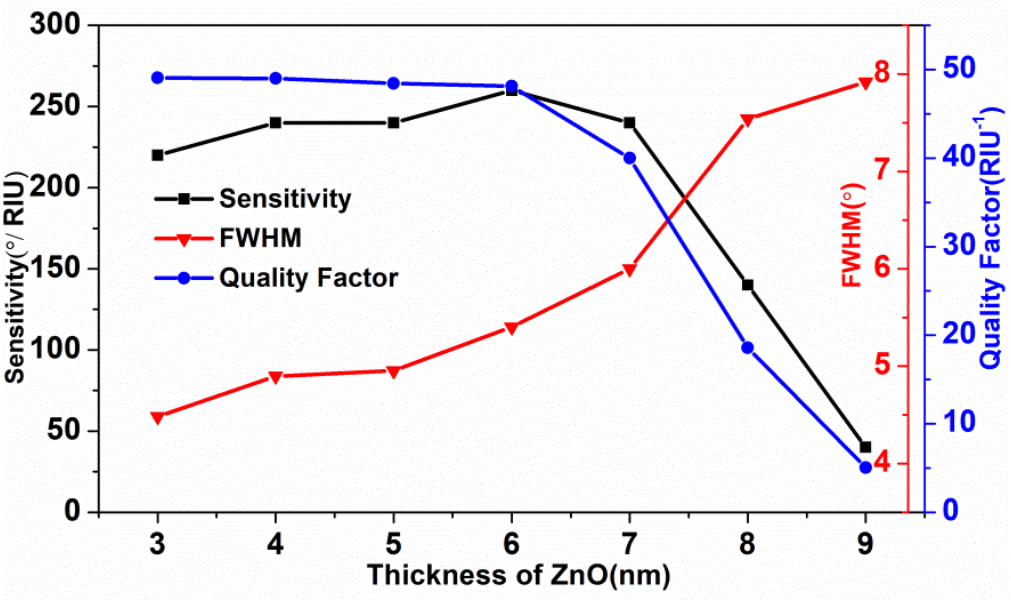


Figure 2.5: Variation of SPR performance parameters for Design III with different thicknesses of ZnO

### 2.3.2 Comparative study of the SPR sensor designs

Figure 2.6 shows the SPR reflectance curves of the optimized designs (Design I, Design II and Design III) for RI variation from 1.330($n_1$)-1.335($n_2$) of sensing medium and Table 2.5 provides a comparative study of the optimized designs. The SPR reflectance curve of Design I (Figure 2.6a) shows a resonance angle shift ($\Delta\Theta_{res}$) of 0.86˚ producing sensitivity, FWHM and QF of 172˚/RIU, 4.26311˚ and 40.35 $RIU^{-1}$ respectively. The SPR reflectance curve of Design II (Figure 2.6b) shows the resonance angle shift ($\Delta\Theta_{res}$) of 1.25˚ producing sensitivity, FWHM and QF of 250˚/RIU, 5.39856˚ and 46.30 $RIU^{-1}$ respectively. In Design II, the use of BlueP-$MoS_2$ heterostructure increases the resonance angle shift resulting in improved sensitivity and QF compared to Design I. The sensitivity enhancement is attributed to the large real part of the RI of BlueP-$MoS_2$ producing an effective increase in the real part of the dielectric constant at trilayer BlueP-$MoS_2$. However, the FWHM of Design II is increased compared to Design I due to an effective increase in the extinction coefficient with the addition of layers of BlueP-$MoS_2$ causing the broadening of the SPR curve. The SPR reflectance curve of Design III (Figure 2.6c) shows the resonance angle shift ($\Delta\Theta_{res}$) of 1.30˚ producing sensitivity, FWHM and QF of 260˚/RIU, 5.40121˚ and 48.14 $RIU^{-1}$ respectively. In Design III, apart from BlueP-$MoS_2$ heterostructure, the introduction of ZnO produces a further increase of the resonance angle shift resulting in improved sensitivity and QF

compared to Design II. The high real part of the RI of ZnO induces an effective increase in the real part of the dielectric constant at an optimal ZnO thickness of 6 nm with 48 nm Au and monolayer BlueP-$MoS_2$ which is attributed to the improved sensitivity. The FWHM of Design III is marginally higher than Design II due to the small value of the extinction coefficient of ZnO producing a marginal effective increment in the extinction coefficient at an optimal thickness of 6 nm. Thus, Design III exhibits the highest sensitivity among Design I and Design II with a sensitivity enhancement of 51.16% and 4% over Design I and Design II respectively. Further Design III also exhibits QF enhancement of 19.3% and 3.97% over Design I and Design II respectively.

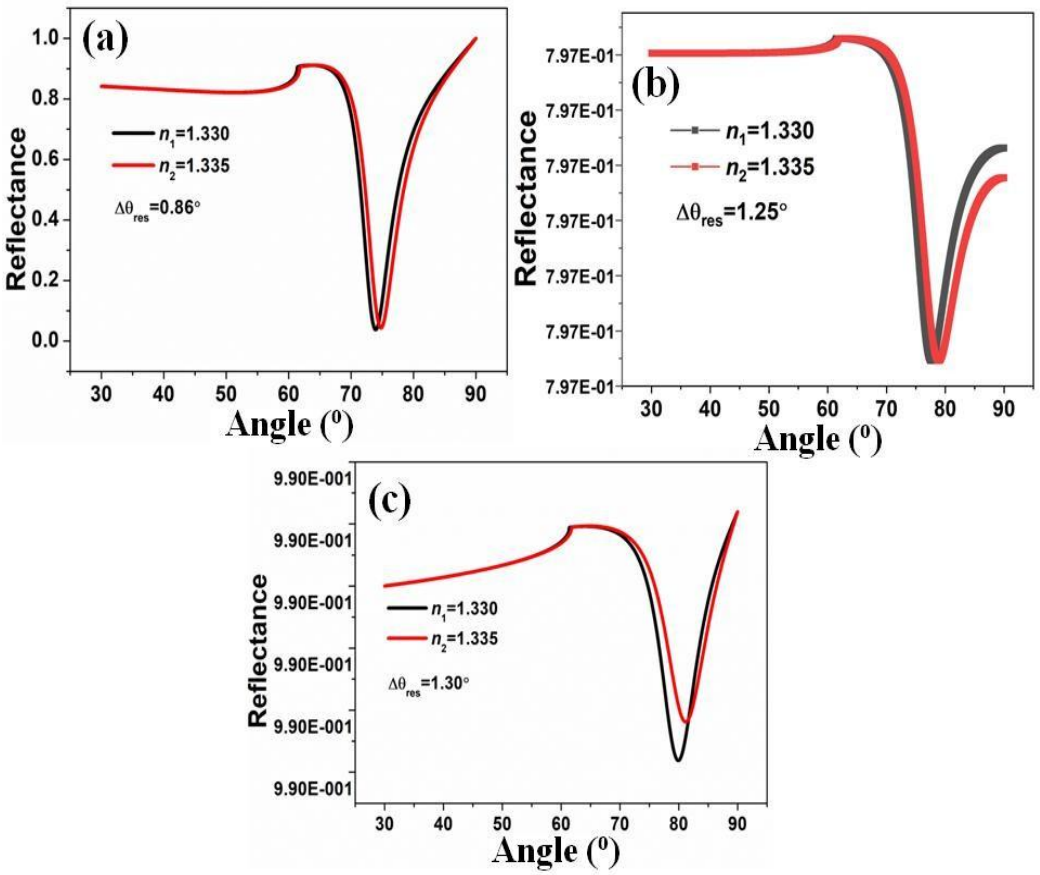


Figure 2.6: SPR reflectance curves of the optimized designs a) Design I b) Design II c) Design III for RI variation from 1.330($n_1$)-1.335($n_2$) of sensing medium

Table 2.5: Comparative study of the optimized designs (Design I, Design II and Design III) for RI 1.330-1.335 of sensing medium

| **SPR sensor design** | **Change in RI of sensing medium ($\Delta n$) (RIU)** | **Change in resonance angle ($\Delta\Theta_{res}$) (°)** | **Sensitivity (°/RIU)** | **FWHM (°)** | **QF ($RIU^{-1}$)** | **Minimum Reflectivity Value (1.330 RI)** | **Minimum Reflectivity Value (1.335 RI)** |
|---|---|---|---|---|---|---|---|
| Design I | 0.005 | 0.86 | 172 | 4.26311 | 40.35 | 0.03791 | 0.04400 |
| Design II | 0.005 | 1.25 | 250 | 5.39856 | 46.30 | 0.79700342 | 0.79700343 |
| Design III | 0.005 | 1.30 | 260 | 5.40121 | 48.14 | 0.99009895 | 0.99009896 |

### 2.3.3 Comparison with recently reported works

The performance of Design III, exhibiting the highest sensitivity among all the SPR sensor designs, is compared with some of the recently reported works. Table 2.6 compares the sensitivities of some of the recently reported SPR sensors with Design III at 633 nm wavelength. It is observed from the table that Design III demonstrates enhanced sensitivity in comparison to a number of reported SPR sensors [28, 32-38]. Table 2.6 also enlists a few SPR sensors which exhibit higher magnitudes of sensitivity than Design III [6, 7, 22, 30, 39]. However, the inherent difficulty in controlling the lattice orientations between 2D nanomaterials or heterostructures with different work functions, energy bandgaps, charge transfer rates, binding energies etc. as reported in the design of these SPR sensors, during experimental synthesis can significantly affect the actual SPR response. In addition, the SPR sensors reported in these works also involve the use of Ag which is prone to oxidation or very low RI prisms such as $CaF_2$ or FK51A which can adversely affect the detection accuracy of the sensor.

Table 2.6: Comparative study with recently reported works

| SPR sensor structure | Wavelength (nm) | S (˚/RIU) | References |
|---|---|---|---|
| SF10/Au/ZnO/Graphene/Sensing medium | 633 | 156.33 | [32] |
| BK7/ZnO/Ag/$BaTiO_3$/$WS_2$/Sensing medium | 633 | 180 | [33] |
| BK7/Au/MXene/$WS_2$/BlackP/Sensing medium | 633 | 190.22 | [34] |
| BK7/Au/Blue P-$MoS_2$ /Sb/Sensing medium | 633 | 194.8 | [35] |
| BK7/Au/Black P/Au/Graphene/Sensing medium | 633 | 218 | [36] |
| BK7/$TiO_2$/Au/MXene /Sb/Sensing medium | 633 | 224.26 | [37] |
| $CaF_2$/ZnO/Au/BlueP-$MoS_2$/Sensing medium | 633 | 235 | [28] |
| FK51A Prism/Ag/Au/MXene/ Sensing medium | 633 | 236 | [38] |
| $CaF_2$/Ag/BlueP-$MoS_2$/ MXene/ Sensing medium | 633 | 302 | [30] |
| FK51A Prism/Ag/$BaTiO_3$/BlueP-$MoS_2$/Sensing medium | 633 | 347.8 | [39] |
| BK7/Ag/Au/$WS_2$/MXene/Sensing medium | 633 | 348 | [6] |
| BK7/Ag/ITO/BlueP-$WS_2$/Graphene/Sensing medium | 633 | 348.8 | [22] |
| BK7/Ag/BlackP/$WS_2$/MXene/ Sensing medium | 633 | 388 | [7] |
| BK7/ZnO/Au/ BlueP-$MoS_2$ /Sensing medium | 633 | 260 | Design III |

## 2.4 Summary

This chapter presents the design of SPR sensors based on multi-layer mathematical models to achieve plasmonic performance enhancement using an optimal combination of promising materials with appropriate design parameters such as RI, layer thickness etc. The sensor performance parameters; viz; Sensitivity, FWHM and QF were studied at an operating wavelength of 633 nm for RI range of 1.33-1.335 RIU of the sensing medium. The effect of the design parameters on the performance parameters of the SPR sensors was studied in detail. Three SPR sensors, viz; Design I, Design II and Design III, were designed based on the three-layer, four-layer and five-layer mathematical models respectively. Design I consists of a prism, Au and sensing medium with an optimized thickness of 55 nm Au demonstrating a sensitivity of 172˚/RIU. Design II consists of a heterostructure of BlueP and $MoS_2$ over the Au layer and sensing medium, producing a sensitivity of 250˚/RIU at an optimized thickness of 54 nm Au and monolayer of BlueP-$MoS_2$ (3 x 0.75 nm). Design III comprises an adhesive layer of ZnO sandwiched between BK7 prism and Au, BlueP-$MoS_2$ heterostructure and sensing

medium, exhibiting a sensitivity of 260˚/RIU at an optimized thickness of 48 nm Au, 6 nm ZnO and a monolayer of BlueP-$MoS_2$ (0.75 nm). A comparative study of the performances of the three SPR sensors is presented at the end of the chapter which demonstrates that Design III exhibited a sensitivity enhancement of 51.16% and 4% over Design I and Design II respectively. Further, Design III also showed a QF enhancement of 19.3% and 3.97% over Design I and Design II respectively.

## Bibliography


[1] Mudgal, N., Yupapin, P., Ali, J., & Singh, G. $BaTiO_3$-graphene-affinity layer–based surface plasmon resonance (SPR) biosensor for pseudomonas bacterial detection. *Plasmonics*, 15: 1221-1229, 2020.

[2] Han, L. & Wu, C. A phase sensitivity-enhanced surface plasmon resonance biosensor based on ITO-graphene hybrid structure. *Plasmonics*, 14(4): 901-906, 2019.

[3] Pal, A., & Jha, A. A theoretical analysis on sensitivity improvement of an SPR refractive index sensor with graphene and barium titanate nanosheets., *Optik*, 231:166378, 2021.

[4] Rahman, M. M., Rana, M. M., Rahman, M. S., Anower, M. S., Mollah, M. A., & Paul, A. K.. Sensitivity enhancement of SPR biosensors employing heterostructure of $PtSe_2$ and 2D materials. *Optical Materials*, 107:110123, 2020.

[5] Liu, N., Wang, S., Cheng, Q., Pang, B., & Lv, J.. High sensitivity in Ni-based SPR sensor of blue phosphorene/transition metal dichalcogenides hybrid nanostructure. *Plasmonics*, 16:1567-1576, 2021.

[6] Ghodrati, M., Mir, A., & Farmani, A.. Sensitivity-Enhanced Surface Plasmon Resonance Sensor with Bimetal/Tungsten Disulfide (WS2)/MXene ($Ti_3C_2T_x$) Hybrid Structure. *Plasmonics*, 17(5):1973-1984, 2022.

[7] Pal, S., Verma, A., Prajapati, Y. K., & Saini, J. P. Sensitive detection using heterostructure of black phosphorus, transition metal di-chalcogenides and MXene in SPR sensor. *Applied Physics A*, 126(10):1-10, 2020.

[8] Maurya, J. B., François, A., & Prajapati, Y. K. Two-dimensional layered nanomaterial-based one-dimensional photonic crystal refractive index sensor. *Sensors*, 18(3): 857, 2018.

[9] Zhu, Y., Murali, S., Cai, W., Li, X., Suk, J. W., Potts, J. R., & Ruoff, R. S. Graphene and graphene oxide: synthesis, properties, and applications. *Advanced Materials*, 22(35): 3906-3924, 2010.

[10] Peng, Q., Wang, Z., Sa, B., Wu, B., & Sun, Z. Electronic structures and enhanced optical properties of blue phosphorene/transition metal dichalcogenides van der Waals heterostructures. *Scientific Reports*, 6(1): 1-10, 2016.

[11] Maurya, J. B., Prajapati, Y. K., Singh, V., & Saini, J. P. Sensitivity enhancement of surface plasmon resonance sensor based on graphene–$MoS_2$ hybrid structure with TiO2–SiO2 composite layer. *Applied Physics A*, 121:525-533, 2015.

[12] Singh, S. & Prajapati, Y. K. $TiO_2$/gold-graphene hybrid solid core SPR based PCF RI sensor for sensitivity enhancement. *Optik*, 224:165525, 2020.

[13] Chiu, N. F., Tu, Y. C., & Huang, T. Y. Enhanced sensitivity of anti-symmetrically structured surface plasmon resonance sensors with zinc oxide intermediate layers. *Sensors*, 14(1): 170-187, 2013.

[14] Brahmachari, K., & Ray, M. Effect of prism material on design of surface plasmon resonance sensor by admittance loci method. *Frontiers of Optoelectronics*, 6(2):185-193, 2013.

[15] Sharma, A. K., Jha, R., & Gupta, B. D. Fiber-optic sensors based on surface plasmon resonance: a comprehensive review. *IEEE Sensors Journal*, 7(8): 1118-1129, 2007.

[16] Bruna, M., & Borini, S. J. A. P. L. Optical constants of graphene layers in the visible range. *Applied Physics Letters*, 94(3): 031901, 2009.

[17] Ouyang, Q., Zeng, S., Jiang, L., Hong, L., Xu, G., Dinh, X. Q., Qian J., He S., Qu J., Coquet P. & Yong, K. T.. Sensitivity enhancement of transition metal dichalcogenides/silicon nanostructure-based surface plasmon resonance biosensor. *Scientific reports*, 6(1): 1-13, 2016.

[18] Sun, P., Wang, M., Liu, L., Jiao, L., Du, W., Xia, F., Liu M, Kong W., Dong L. & Yun, M. Sensitivity enhancement of surface plasmon resonance biosensor based on graphene and barium titanate layers. *Applied Surface Science*, 475: 342-347, 2019.

[19] Daniyal, W. M. E. M. M., Fen, Y. W., Abdullah, J., Sadrolhosseini, A. R., Saleviter, S., & Omar, N. A. S. Exploration of surface plasmon resonance for sensing copper ion based on nanocrystalline cellulose-modified thin film. *Optics express*, 26(26): 34880-34893, 2018.

[20] Ruan, B., You, Q., Zhu, J., Wu, L., Guo, J., Dai, X., & Xiang, Y. Improving the performance of an SPR biosensor using long-range surface plasmon of Ga-doped zinc oxide. *Sensors*, 18(7), 2098, 2018.

[21] Maharana, P. K., Padhy, P., & Jha, R. On the field enhancement and performance of an ultra-stable SPR biosensor based on graphene. *IEEE Photonics Technology Letters*, 25(22): 2156-2159, 2013.

[22] Han, L., Ding, H., Landry, N. N. A., Hua, M., & Huang, T. Highly sensitive SPR sensor based on Ag-ITO-BlueP/TMDCs-graphene heterostructure. *Plasmonics*, 15:1489-1498, 2020.

[23] Alagdar, M., Yousif, B., Areed, N. F., & Elzalabani, M. Improved the quality factor and sensitivity of a surface plasmon resonance sensor with transition metal dichalcogenide 2D nanomaterials. *Journal of Nanoparticle Research*, 22:1-13, 2020.

[24] Paliwal, A., Gaur, R., Sharma, A., Tomar, M., & Gupta, V. Sensitive optical biosensor based on surface plasmon resonance using ZnO/Au bilayered structure. *Optik*, 127(19): 7642-7647, 2016.

[25] Duenow, J. N., Gessert, T. A., Wood, D. M., Barnes, T. M., Young, M., To, B., & Coutts, T. J. Transparent conducting zinc oxide thin films doped with aluminum and molybdenum. *Journal of Vacuum Science & Technology A: Vacuum, Surfaces, and Films*, 25(4): 955-960, 2007.

[26] Sexton, B. A., Feltis, B. N., & Davis, T. J. Characterisation of gold surface plasmon resonance sensor substrates. *Sensors and Actuators A: Physical*, 141(2): 471-475, 2008.

[27] Kushwaha, A. S., Kumar, A., Kumar, R., Srivastava, M., & Srivastava, S. K. Zinc oxide, gold and graphene-based surface plasmon resonance (SPR) biosensor for detection of pseudomonas like bacteria: A comparative study. *Optik*, 172: 697-707, 2018.

[28] Singh, S., Sharma, A. K., Lohia, P., & Dwivedi, D. K. Theoretical analysis of sensitivity enhancement of surface plasmon resonance biosensor with zinc oxide and blue phosphorus/$MoS_2$ heterostructure. *Optik*, 244: 167618, 2021.

[29] Srivastava, A., & Prajapati, Y. K. Performance analysis of silicon and blue phosphorene/$MoS_2$ hetero-structure based SPR sensor. *Photonic Sensors*, 9: 284-292, 2019.

[30] Pal, S., Pal, N., Prajapati, Y. K., & Saini, J. P. Sensitivity analysis of surface Plasmon resonance biosensor based on Heterostructure of 2D BlueP/$MoS_2$ and MXene. *Layered 2D advanced materials and their allied applications; Inamuddin, Boddula R., Ahamed M. I., Asiri A. M. (Eds.); Scrivener Publishing LLC: Beverly, USA*: 103-129, 2020.

[31] Sharma, A. K., & Pandey, A. K. Blue phosphorene/$MoS_2$ heterostructure based SPR sensor with enhanced sensitivity. *IEEE Photonics Technology Letters*, 30(7): 595-598, 2018.

[32] Pal, S., Prajapati, Y. K., & Saini, J. P. Influence of graphene's chemical potential on SPR biosensor using ZnO for DNA hybridization. *Optical Review*, 27(1): 57-64, 2020.

[33] Kumar, A., Yadav, A. K., Kushwaha, A. S., & Srivastava, S. K. A comparative study among $WS_2$, $MoS_2$ and graphene based surface plasmon resonance (SPR) sensor. *Sensors and Actuators Reports*, 2(1): 100015, 2020.

[34] Srivastava, A., Verma, A., Das, R., & Prajapati, Y. K. A theoretical approach to improve the performance of SPR biosensor using MXene and black phosphorus. *Optik*, 203, 163430, 2020.

[35] Singh, M. K., Pal, S., Prajapati, Y. K., & Saini, J. P. Sensitivity improvement of surface plasmon resonance sensor on using BlueP/$MoS_2$ heterostructure and antimonene. *IEEE Sensors Letters*, 4(7):1-4, 2020.

[36] Singh, Y., Paswan, M. K., & Raghuwanshi, S. K. Sensitivity enhancement of SPR sensor with the black phosphorus and graphene with bi-layer of gold for chemical sensing. *Plasmonics*, 16: 1781-1790, 2021.

[37] Raikwar, S., Srivastava, D. K., Saini, J. P., & Prajapati, Y. K. 2D-antimonene-based surface plasmon resonance sensor for improvement of sensitivity. *Applied Physics A*, 127: 1-8, 2021.

[38] Srivastava, A., & Prajapati, Y. K. Surface plasmon resonance (SPR)-based biosensor using MXene as a BRE layer and magnesium oxide (MgO) as an adhesion layer. *Journal of Materials Science: Materials in Electronics*, 33(11): 8519-8528, 2022.

[39] Setareh, M., & Kaatuzian, H. Sensitivity enhancement of a surface plasmon resonance sensor using Blue Phosphorene/$MoS_2$ hetero-structure and barium titanate. *Superlattices and Microstructures*, 153, 2021.